Mesoporous textured Fe-N-C electrocatalysts as highly efficient cathodes for proton exchange membrane fuel cells

Srinu Akula[a], Marek Mooste[a], Barr Zulevi[b], Sam McKinney[b], Arvo Kikas[c], Helle-Mai Piirsoo[c], Mihkel Rähn[c], Aile Tamm[c], Vambola Kisand[c], Alexey Serov[d,*], Erin B. Creel[d], David A. Cullen[d], Kenneth C. Neyerlin[e], Hao Wang[e], Madeleine Odgaard[f], Tatyana Reshetenko[g], Kaido Tammeveski[a*]

[a] *Institute of Chemistry, University of Tartu, Ravila 14a, 50411 Tartu, Estonia*

[b] *Pajarito Powder, LLC, 3600 Osuna Rd NE Ste 309, Albuquerque, NM, 87109 USA*

[c] *Institute of Physics, University of Tartu, W. Ostwald Str. 1, 50411 Tartu, Estonia*

[d] *Oak Ridge National Laboratory, 1 Bethel Valley Road, Oak Ridge, TN, 37830, USA*

[e] *Chemistry and Nanoscience Center, National Renewable Energy Laboratory, Golden, CO, 80401, USAf*

[f] *IRD Fuel Cells, LLC, 8500 Washington St. NE, Albuquerque, NM, 87113, USA*

[g] *Hawaii Natural Energy Institute, University of Hawaii, Honolulu, HI 96822, USA*

ABSTRACT

A new platinum group metal (PGM)-free proton exchange membrane fuel cell (PEMFC) cathode catalyst material, synthesized using the VariPore™ method by Pajarito Powder, LLC, is characterized for its structure and activity. The physico-chemical analysis of the mesoporous iron-nitrogen-carbon (Fe-N-C) catalyst shows a mesoporous carbon material effectively doped with iron and nitrogen. The material has an average pore size of 7-8 nm and high specific surface area The Fe-N-C catalyst exhibits high electrocatalytic activity for oxygen reduction reaction (ORR) in 0.5 M H_2SO_4 electrolyte with high half-wave potentials and sustainable electrochemical stability over 10,000 repeated potential cycles with insignificant losses in their activities. As cathode catalysts in a PEMFC, the Fe-N-C material delivers remarkably good fuel cell performance at low overpotential approaching that of the commercial Pt catalyst. The high ORR electrocatalytic activity of these Fe-N-C catalysts is credited to the synergy between nitrogen-moieties, specifically pyrrolic-N, pyridinic-N, and graphitic-N, and iron in addition

---

[*] Corresponding author. Tel.: +372 7375168; E-mail: kaido.tammeveski@ut.ee (K. Tammeveski).
E-mail: serov@h2pgm.com (A. Serov, previously associated with Pajarito Powder, LLC)

to the high mesoporosity that facilitate an effective reaction path in boosting the electrocatalytic activity and stability.

***Keywords*:** Electrocatalysis; Fe-N-C catalyst; mesoporous carbon; nitrogen doping; oxygen reduction reaction; Proton-exchange membrane fuel cell.

1. Introduction

Propelled by declining reserves of fossil fuels, alternative energy conversion and storage devices are in critical need. Proton exchange membrane fuel cells (PEMFCs) exhibit high energy efficiency and low environmental concern due to their zero pollutant emissions [1,2]. The oxygen reduction reaction (ORR), the sluggish cathodic reaction of a PEMFC is typically catalysed by Pt nanoparticles supported on carbon (Pt/C) with high areal loading; hence, cost remains one of the critical obstacles to the broad dissemination of this technology [3,4]. Though Pt/C is the state-of-the-art ORR catalyst, it undergoes degradation due to agglomeration, Pt ripening, and carbon corrosion, leading to a decline in the electrocatalytic activity/stability and diminished overall PEMFC performance [5,6]. Numerous studies have reported alternatives to Pt-based electrocatalysts for catalysing ORR. These platinum group metal (PGM)-free alternatives include heteroatom (N, O, P, S, F)-doped carbons and non-precious metal catalysts [7-16]. Transition metals coordinated to nitrogen-doped carbon catalysts (M−N−C) show the most promising ORR activity, with best-in-class PGM-free catalysts now approaching baseline Pt/C catalyst performance both in alkaline and acidic media [17-19]. However, to date, the stability of the Fe-N-C based catalysts in PEMFCs is limited significantly compared to the Pt/C counterparts [20-24]. Very recently, researchers have provided some insight on the catalytic active sites and durability of the Fe-N-C catalysts through Operando Spectroscopy, X-band EPR spectra, phase-corrected FT-EXAFS, and ^{57}Fe Mössbauer Spectra for better understanding about the factors affecting the stability loss [25-

29]. Although the mechanism for the enhanced ORR activity of M-N-C catalysts continues to be debated, many studies agree that Fe−N_x sites are the most active and favourable for ORR in acidic medium [30-33]. In contrast, Fe-N_x and iron particles together exhibit good ORR activity in alkaline medium [34].

Several studies have explored the morphology, particle size, structure/textures, and chemical states of Fe-N-C catalyst to increase the number of active sites and the ORR activity [35-39]. However, marked improvements in the catalyst performance are needed to make these materials commercially feasible. While there have been notable ORR activity enhancements, further improvements are hindered by the lack of molecular-level understanding or control of the iron active sites [40,41]. Fe-N-C materials are typically prepared by the high-temperature pyrolysis of nitrogen-rich compounds in the presence iron salts, Fe porphyrins, or phthalocyanines accompanied by a metal-organic framework (MOF) or carbon supports [42-48]. The non-specific nature of pyrolysis results in a broad assortment of iron-nitrogen environments along with extended solid iron phases in the resulting Fe-N-C catalysts [49-51]. The poor synthetic control coupled with inconsistency in the synthetic methods has led to uncertainty about the local structure of the iron active sites responsible for ORR and hampers rational improvements to catalytic performance [52].

The easiest and most efficient approach to generating a greater number of active sites is by enhancing the microporous surface area since ORR-active sites are primarily located in micropores [53-55]. Constructing an integrated micro-/meso-/macro-porous carbon with high surface area is considered to be the most promising strategy to increase the utilisation of catalytically active sites through shortening the diffusion paths of reactants and products [56,57]. Pajarito Powder, LLC has successfully scaled-up procedures for producing highly porous Fe-N-C catalysts through the VariPore™ method [58-61]. This work focuses on the characterisation of this novel commercially available PGM-free catalyst (Fe-N-C; Pajarito

Powder, LLC product codes 230-002-C29, 230-002-C30, and 230-002-C31) using several physico-chemical characterisation methods. Additionally, the material's electrocatalytic ORR activity is investigated with the rotating disk electrode (RDE) method. These catalysts exhibit excellent activity in 0.5 M H_2SO_4 electrolyte, viable electrochemical stability, and outstanding performance in PEMFC as efficient cathodes. Hence, this study begins a new era in PEMFC technology with new commercially viable Fe-N-C catalysts.

2. Experimental

Fe-N-C electrocatalysts (product codes: 230-002-C29, 230-002-C30 and 230-002-C31) were produced by Pajarito Powder, LLC and used without further modification [58-60].

2.1. Physico-chemical characterisation of catalysts

The physico-chemical characterisation of the catalyst materials was carried out by scanning electron microscope (SEM), Helios NanoLab 600 (FEI Company) using 10 keV primary electrons energy composed with energy dispersive X-ray spectroscopy (EDS) using an INCA Energy 350 (Oxford Instruments) detector. Secondary electron (SE) and annual dark field (ADF) images were recorded on a JEOL NEOARM operated at 80 kV and equipped with a dual 100 mm^2 solid state detectors for EDS. STEM characterisation was also performed at 200 kV using a Cs-probe corrected FEI Titan Themis 200 (scanning) transmission electron microscope equipped with a SuperX EDX system (Bruker). N_2 physisorption measurements – Autosorb-3B (Quantachrome); dynamic light scattering (DLS) – Zetasizer Nano series (Malvern); X-ray photoelectron spectroscopy (XPS) – non-monochromatic twin anode X-ray tube (Thermo XR3E2) with the characteristic energy of 1486 eV (Al K_α) and an electron energy analyser SCIENTA SES 100; X-ray diffraction (XRD) – Miniflex 600 (Rigaku) and Raman spectroscopy – DXR SmartRaman (Thermo Scientific) with 532 nm laser. 50 mg of catalyst was added to 15 mL of 2-propanol and sonicated in an ultrasonication bath for 30 min for DLS inspection. The pore size distribution (PSD) was determined by the Barrett-Joyner-Halenda (BJH) method.

2.2. Electrochemical measurements

The surface of the 0.13 cm^2 glassy carbon (GC) working electrode was smoothened by 1, 0.3 and 0.05 μm sized alumina slurry (Buehler) and subsequent washing in Milli-Q water and 2-propanol. 2 mg of the catalyst material dispersed in 495 μL 2-propanol, 495 μL Milli-Q water, and 10 μL Nafion® ionomer solution (5 wt%, Sigma-Aldrich) followed by 1 h of sonication to prepare the suspensions of the catalysts. An aliquot from the suspension was pipetted on the cleaned GC surface, to attain a catalyst loading of 0.2 mg cm^{-2} and dried in an oven at 60 °C. In addition, 46% Pt/C (Tanaka Kikinzoku Kogyo, Japan) was used to compare the ORR results. In a similar run, 1.2 mg of 46% Pt/C dispersed in 990 μL Milli-Q water and 10 μL Nafion® ionomer solution (5 wt%, Sigma-Aldrich) followed by 0.5 h of sonication. 7 μL of the suspension was dropped on the GC surface to obtain 30 μg_{Pt} cm^{-2} loading.

The electrochemical experiments were carried out in a standard three-electrode electrochemical cell comprising O_2-(99.999%, Linde) or Ar-(99.999%, Linde) saturated 0.5 M H_2SO_4 (purity ≥95%, Sigma-Aldrich) solution at room temperature. Saturated calomel electrode (SCE) coupled with salt bridge was acted as a reference electrode, but all the potentials are conveyed with respect to the reversible hydrogen electrode (RHE) scale for the fair comparison. A carbon rod (diameter of 3 mm) isolated by a glass frit was acted as an auxiliary electrode. The rotating disk electrode (RDE) measurements and cycling stability tests were performed by PGSTAT30 Autolab potentiostat/galvanostat (Eco Chemie B.V., The Netherlands), utilising General Purpose Electrochemical System software. The stability tests were conducted by 10,000 recurrent potential cycles in the potential window of 0.6 – 1.0 V vs. RHE at a scan rate of 50 mV s^{-1} in O_2-saturated 0.5 M H_2SO_4 electrolyte.

2.3. Proton exchange membrane fuel cell testing

The catalyst-coated membranes (CCMs) with active area of 25 cm^2 were manufactured at IRD Fuel Cells, LLC using a proprietary membrane material and a digital spray coating method. As an anode catalyst, we used Pt/C with loading of 0.2 mg_{Pt} cm^{-2}. The cathode loading of PGM-free catalyst was 2.5 mg_{cat} cm^{-2}. The membrane-electrode assemblies (MEAs) were obtained by hot-pressing the CCM, gas diffusion layers (GDLs) and gaskets materials at 140 °C and 2400 lbs of force pressure for 4 min. In this work we used 22BB SGL and Freudenberg H23C8 GDLs. Both GDLs have thickness of 220±20 μm, hydrophobic treatment by polytetrafluoroethylene (PTFE) and microporous layer (MPL). The gasket thickness was 155 μm for the anode and 255 μm for the cathode, ensuring a compression ratio of 20%.

All MEA samples were tested using a small-scale differential cell with a 50 cm^2 flow field with 14-channel serpentine design [62]. The anode and cathode of the MEA were covered by impermeable gaskets to reduce the active area to 5 cm^2 immediately upstream at the cell outlet. The differential cell with high flow reagent supply ensured a lack of flooding and good mass transport, while the fully humidified inlet gas avoided ionomer drying effects and provided proper electrodes and membrane humidification.

Polarization or IV curves were recorded at H_2/O_2 and H_2/air gas configurations using Fuel Cell Technology test stations. The IV curve measurements were accompanied by detecting cell resistance (R) using the high frequency resistance (HFR) method when a small perturbation signal at a single high frequency of 3 kHz was applied to the electronic load and the resulting magnitude of phase and voltage/current responses were detected by a frequency analyser. For all tests the cell temperature was 80 °C and the reagents were supplied at 100% humidity and 150 kPa back pressure. The anode and cathode flow rates were 0.5 and 1.0 L min^{-1} for H_2/O_2 experiments. For the H_2/air configuration the gases were fed at 0.7 and 1.7 L min^{-1}. IV curves with O_2 and air as cathode feed gases were used to separate activation (η_{act}), ohmic (η_{Ohm}) and mass transport (η_{MT}) overpotentials as described previously [63,64]. The detailed information on the MEA evaluation and the durability test protocols (Table S1 and Fig. S1) are presented in the Supporting Information.

3. Results and discussion

3.1. Structural characterisations and composition analysis

SEM images in Fig. S2 show the exterior morphology of the three Fe-N-C catalysts. Most of the material is homogeneous in each catalyst with considerable roughness. Among the catalysts, the 230-002-C30 catalyst is most homogeneous in particle size distribution (Fig. S2f-j) at different magnifications. There are also a few smooth and larger particles in 230-002-C29 and 230-002-C31 catalysts as shown in Fig. S2a-e and S1k-o, respectively. The SEM-EDS elemental composition analysis showed the presence of both iron (0.6–1 wt.%) and nitrogen (6–8 wt.%), indicating successful doping. Minor deposits of Si and Zn are also noticed, which were generated from the synthesis method. The comprehensive elemental compositions of the catalysts are listed in Table S2 (Supporting information).

The XRD pattern in Fig. 1a shows that the Fe-N-C materials exhibit characteristic graphitic carbon peaks at $2\theta \approx 26.2–26.6°$ and at $2\theta \approx 41–46°$. The first carbon peak (≈ 26.5°) is attributed to (002) 2H and (111) 3R graphite, while the second (≈ 46°) matches (100) and (101) 2H along with (010) and (110) 3R. The broad XRD peaks indicate that the materials are heterogeneous and disordered graphitic frameworks. The slightly disordered structure, besides the high 3R graphite content, specifies the Fe-N-C catalysts comprise substantial defects (Table 1).

Raman spectra (Fig. 1b) show the presence of two wide bands, which are characteristic of the carbon-based materials – graphitic carbon (G) and disordered carbon (D) peaks located at ~1595 and ~1350 cm^{-1}, respectively. The latter becomes noticeable when the structure is disordered and indicates that the material is quite amorphous. The ratio of D and G peak intensities (I_D/I_G) is 0.96, 1.02 and 0.98 for 230-002-C29, 230-002-C30, and 230-002-C31 catalysts (Table 1), respectively. The disordered structure creates more defects and induces charge delocalisation, spin orientation, and a reduction in the band gap in the catalysts [65]. These defects induce active sites that are highly favourable for ORR electrocatalysis

N_2 physisorption was used to analyse textural characteristics with the pore size distribution shown in Fig. 1c, d. The catalysts exhibit a characteristic hysteresis loop of the N_2 adsorption-desorption isotherms in the relative pressure range ($0.6 < P/P_o < 0.9$) due to the mesoporous nature of the Fe-N-C catalysts. Characteristic features of Type H4 or H2b isotherm are observed, which are associated with mesoporous carbon [66]. Fe-N-C materials have a typical pore size around 6-8 nm (inset Fig. 1c). In addition, the high BET surface area of 700, 725 and 640 $m^2\ g^{-1}$ exhibited by 230-002-C29, 230-002-C30 and 230-002-C31 catalysts, respectively (Table 1), shows the possibility of a large number of catalytically active-centres. The catalyst particle size distribution obtained by DLS is shown in Fig. 1d with two maxima at 140 and 500-700 nm. The average particle size is 520, 355, and 270 nm for 230-002-C29, 230-002-C30 and 230-002-C31 catalysts, respectively (refer Table 1 for values).

The morphology and nanostructures are investigated by using aberration-corrected STEM as shown in Fig. 2. Figure 2a-c contains secondary electron (SE)-STEM images for 230-002-C29, 230-002-C30 and 230-002-C31 catalyst respectively wherein, the crumpled porous layered structures are observed. High-resolution annular dark field (ADF)-STEM images display dispersed bright spots corresponding to Fe single atoms over the entire carbon frameworks of 230-002-C30 catalyst as shown in Fig. 2d-f. Notably, the uniform distribution of cluster-free Fe atoms in the 230-002-C30 catalyst (Fig. 2d-f) imply the atomic Fe sites are likely coordinated with N atoms. The well-defined porous peripheries and wide-spread carbon layers revealed that the adopted synthesis route plays a significant role in establishing highly porous nanostructured catalysts. There are no Fe-based nanoparticles or clusters observed in the entire porous nanostructure, suggesting Fe-based nanoparticles or clusters produced throughout the pyrolysis might be eradicated successfully with acid etching and with only single Fe atoms remaining. Additional studies are needed to confirm the absence of Fe-based nanoparticles or clusters. Many crumpled porous carbon nanosheets were observed for 230-002-C29 and 230-002-C31 catalysts as shown in Fig. S3a-d and 2i-l, respectively. Remarkably, widespread, and relatively highly porous carbon networks are found for 230-002-C30 catalyst shown in Fig. S3e-h. These morphological characteristics corroborate the data obtained from N_2 physisorption. STEM elemental mapping in Fig. S4a-e further showed the uniform distribution of N, O and Fe in the 230-002-C29 catalyst structure. Hence, the selected synthesis route promotes the formation of atomically-dispersed Fe atoms, instead of Fe aggregation, during a scalable high-temperature treatment. The unique textural assets might increase the density of atomically dispersed Fe-N active sites to enhance the ORR electrocatalytic activity.

XPS survey spectra for Fe-N-C catalysts (Fig. 3a-c) reveal three distinct peaks corresponding to C 1s (~285 eV), O 1s (~532 eV), and N 1s (~400 eV) with the respective surface concentrations listed in Table S3. Insets to Fig. 3a-c show the deconvoluted XPS spectra in the C 1s region. The deconvolution of the detailed N 1s spectrum (Fig. 3d, e, f) shows that the most ORR active N-species pyrrolic-N, pyridinic-N and graphitic-N exist in substantial concentrations (Table S3). N atoms in pyridinic-N situated at the edges of layers with each N atom attached to two carbons of six-membered rings are active for ORR due to their donation of their lone pair of electrons. The electron donation polarises the O=O bond, activating O_2 for reduction [67]. Pyrrolic-N atoms, a member of five-membered heterocyclic rings, are bonded to two carbon atoms and donate two p electrons to the aromatic system. Graphitic-N is integrated within the graphitic matrix by substituting for a carbon atom and tends to create high ORR-active centres [68]. Fe-N-C active sites have improved the ORR activity due to substantial oxygen adsorption, subsequential cleavage and well-established synergy between the active forms of nitrogen and iron [69].

3.2. Oxygen reduction reaction (ORR) studies

The RDE method was employed to give an initial assessment of the Fe-N-C catalyst materials' electrocatalytic ORR activity in aqueous 0.5 M H_2SO_4 electrolyte. The cyclic voltammograms (CVs) and linear sweep voltammograms (LSVs) of the catalysts are shown in Fig. 4a, b. The catalysts exhibit the characteristic ORR peak in the CVs in O_2-saturated 0.5 M H_2SO_4 and the corresponding ORR peak potentials (E_p) are indicated in Fig. 4a. The 230-002-C30 catalyst exhibits the highest E_p among the three catalysts, which is ascribed to the hierarchical porous structure that might facilitate the faster ORR kinetics. The electrocatalytic ORR activity of these catalysts is further explored through LSVs (Fig. 4b) to validate the data obtained from CVs; the corresponding half-wave potentials ($E_{1/2}$) for the three Fe-N-C catalysts as well as the commercial Pt/C catalyst are indicated in Fig. 4b. The Fe-N-C catalysts show comparable ORR activity with the Pt/C catalyst. The 230-002-C30 catalyst exhibits better activity than other two Fe-N-C catalysts with the highest $E_{1/2}$ value (0.76 V) as expected from the CV data and improved catalyst structure. The 230-002-C30 has the highest density of active sites and the hierarchal textural properties that we expected to give higher activity. The that direct correlation of catalyst performance obtained in RDE experiments and fuel cell tests is complicated and would require additional experiments to deconvolute input of individual parameters, i.e. porosity, hydrophobicity, surface chemistry, etc. Tafel plots were constructed from the LSVs to evaluate the ORR kinetics of the developed catalysts (Fig. 4c). The 230-002-C30 catalyst exhibits the fastest kinetics as shown by its lowest slope (-88 mV dec^{-1}) and similarity to the commercial Pt/C catalyst's Tafel slope (-83 mV dec^{-1}). The Tafel slope for the 230-002-C29 catalyst is -95 mV dec^{-1}, and the slope for the 230-002-C31 catalyst is -90 mV dec^{-1}, both showing promising ORR activity. The electro-kinetics of the Fe-N-C catalysts are further explored using hydrodynamic voltammograms at different electrode rotation rates (Fig. 5). The limiting current densities increase with rotational speeds as the rotational speed increases the O_2 diffusion rate to the electrolyte−electrode interface. The hydrodynamic voltammograms for each Fe-N-C catalyst are shown in Fig. 5a-c respectively for the 230-002-C29, 230-002-C30, and 230-002-C31 catalysts. The Koutecky-Levich (K−L) plots for catalysts at various potentials are presented in Fig. 5d-f, and the number of electrons transferred (*n*) during the ORR process is calculated using the K−L equation:

$$\frac{1}{j} = \frac{1}{j_k} + \frac{1}{j_d} \qquad (1)$$

where j is the overall measured ORR current density, j_k is kinetic current density, j_d is diffusion-limited current density, and B is the Levich parameter calculated from the following equations:

$$j_d = B\omega^{1/2} \qquad (2)$$

$$B = 0.62nFC_{O_2}D_{O_2}{}^{2/3}\,\upsilon^{-1/6} \qquad (3)$$

where F is the Faraday constant (96,485 C mol^{-1}), C_{O2} is the bulk oxygen concentration in the 0.5 M H_2SO_4 electrolyte (1.13×10^{-6} mol cm^{-3}), D_{O2} is the diffusion coefficient of molecular O_2 (1.8×10^{-5} cm^2 s^{-1}), ν is the kinematic viscosity of the electrolyte (0.01 cm^2 s^{-1}), ω is the rotation rate of the disk electrode (with units of rad s^{-1}). The linearity of the K-L plots for ORR on the electrocatalysts suggests first-order reaction kinetics towards O_2 concentration Fig. 5d-f. The *n* value was found to be 3.90, 3.98, and 3.95 for 230-002-C29, 230-002-C30, and 230-002-C31 catalysts, respectively. This indicates that the catalysts exhibit a nearly four-electron pathway for ORR and the reaction product is H_2O.

One of the major hurdles for long-term PEMFC operation is the electrochemical stability of the ORR electrocatalyst. The Fe-N-C catalysts are subjected to rigorous tests up to 10,000 repeated potential cycles in 0.5 M H_2SO_4 electrolytic medium to evaluate their stability. Remarkably, these catalysts retain their electrochemical ORR behaviour with well-defined kinetic and diffusion-controlled regions even after 10,000 potential cycles as shown in Fig. 6a-

c. The 230-002-C30 catalyst shows higher stability over 10,000 potential cycles with only ~30 mV negative shifts in $E_{1/2}$ value compared to 80 and 40 mV shifts for 230-002-C29 and 230-002-C31 catalysts, respectively. The hierarchal architectures and incredible synergistic effect of the Fe-N-C moiety are believed to play pivotal role in the outstanding stability.

3.3. Proton exchange membrane fuel cell analysis

Finally, the electrocatalysts were evaluated for their performance in a single cell PEMFC. Fig. 7 shows the polarization and power density curves as functions of current density recorded in 5 cm^2 differential cells using O_2 or air as the cathode feed gas. For comparison purposes we also include data for PEMFC operation with the Pt/C electrocatalyst with loading of 0.1 mg_{Pt} cm^{-2} for both electrodes. The results show that samples 230-002-C30 and 230-002-C31 demonstrate the highest performance in H_2/O_2 conditions with a peak power density (P_{max}) of 0.837 W cm^{-2}, while the MEA with the 230-002-C29 electrocatalyst exhibits the lowest performance (P_{max} = 0.645 W cm^{-2}). In the kinetic region (cell voltage > 0.8 V) in H_2/O_2 operating conditions, the generated current density of PGM-free MEAs is excellent by virtue of the high ORR activity of PGM-free catalysts. The enlargement of Fig. 7 is recreated to better distinguishing and presented as Fig. S5 in the SI. Switching the cathode feed gas from O_2 to air results in noticeable performance decline at cell voltages below 0.75 V. Interestingly, the 230-002-C29 sample has the best performance among the three Fe-N-C catalysts in the H_2/air configuration. A comparison of the electrochemical parameters of the catalysts in this study with other catalysts in literature reports are tabulated in Table S4 (Supporting Information). The catalysts developed in this study exhibit higher power densities than many studies reported (Table S4).

To understand the performance, we estimate activation, ohmic and mass transport overpotentials in the MEA and compare those of the Fe-N-C catalysts to those of the Pt catalyst (Fig. 8). Activation losses of the PGM-free samples are determined to be only slightly higher than for the Pt sample at low current density, but a further increase in operating current causes a drastic growth in η_{act} (Fig. 8a). The sample 230-002-C29 has the highest values of activation overpotential, which explains its poorer performance in H_2/O_2 conditions (Fig. 7). The high activation voltage losses of PGM-free MEAs compared to the Pt sample are previously reported and can be attributed to lower active site density and accessibility [70]. A comparison of the mass transport losses clearly shows that PGM-free MEAs had higher mass transport overpotentials (η_{MT}) than the Pt cell (Fig. 8b). The 230-002-C29 sample has the lowest η_{MT} among the PGM-free samples, which results in better performance of this sample in H_2/air conditions (Fig. 7). Generally, the high η_{MT} for PGM-free materials is explained by the significantly thicker catalyst layer of 50-70 μm compared to 4-8 μm for Pt electrode structures. The thick PGM-free cathode electrode limits efficient O_2 mass transport and water management. The lower ohmic overpotential of the PGM-free versus the Pt samples (Fig. 8c) is due to the advanced electrode coating method developed by IRD; all PGM-free MEAs have low cell resistances of 45-55 mOhm cm^2 whereas the Pt MEA has a cell resistance of 75 mOhm cm^2 (Fig. 8d). The electrochemical characterisation reveals that activation and mass transport losses still determine the PGM-free MEA performances. However, a comparison of our previous results reported in ref. [70] with Figs. 7 and 8 demonstrate that the new generation of PGM-free electrocatalysts and advanced CCM coating techniques could significantly improve the PGM-free MEA performance by decreasing η_{act} and η_{MT}. In order to evaluated durability of most stable electrocatalyst (230-002-C30) in RDE conditions, the experiment was performed as recommended by US DOE ElectroCat consortium protocol (Fig. S5 and description in SI). It was found that voltage decay at 0.8 A cm^{-2} was equal 70 mV, which is still higher than US DOE target of 30 mV (Ref. [71]). The additional systematic durability study of novel R&D PGM-free catalysts made by VariPore™ method are planned to be performed and presented to the community.

4. Conclusions

Non-precious metal catalyst materials with Fe-N-C moieties exhibit high specific surface area and high mesoporosity produced by the VariPore™ method. The XRD analysis and Raman spectroscopy detected defects in the Fe-N-C catalysts that are beneficial for ORR performance. The designed catalysts consist around 1 wt.% of iron by SEM-EDS, and the coexistence of all the active forms of nitrogen dopants were detected by XPS. The recently commercially available Fe-N-C catalysts explored in this study exhibited excellent electrocatalytic activity towards the ORR in acidic electrolyte with high half-wave potentials and promising electrochemical stability over 10,000 repeated potential cycling. PEMFC MEAs made with the Fe-N-C cathode catalysts delivered high power and current densities approaching the commercial Pt catalyst baseline. Therefore, the commercially available Fe-N-C electrocatalysts can be used in the community for benchmarking of new PGM-free ORR materials.

Declaration of competing interest

The authors declare that they have no known competing financial interests or personal relationships that could have appeared to influence the work reported in this paper.

Acknowledgements

The present work was financially supported by the Estonian Research Council (grants PRG723, PRG4, MOBJD671) and M-ERA.Net project “C-MOF.cell” (SLTKT20445). This research was also supported by the EU through the European Regional Development Fund (TK141, “Advanced materials and high-technology devices for energy recuperation systems” and TK134, “Emerging orders in quantum and nanomaterials”). A. Serov, M. Odgaard, B. Zulevi and T. Reshetenko gratefully acknowledge financial support from the US DOE EERE (DE-EE0008419 “Active and Durable PGM-free Cathodic Electrocatalysts for Fuel Cell Application”). A. Serov and E. Creel gratefully acknowledge financial support from the Oak

Ridge National Laboratory SEED 10609 project "Single-Atom Catalysts for CO_2 Conversion". T. Reshetenko is grateful to funding from US Office of Naval Research (N00014-18-1-2127). Aberration-corrected STEM was conducted at the Center for Nanophase Materials Sciences, which is a DOE Office of Science User Facility.

References

[1] D.A. Cullen, K.C. Neyerlin, R.K. Ahluwalia, R. Mukundan, K.L. More, R.L. Borup, A.Z. Weber, D.J. Myers, A. Kusoglu, New roads and challenges for fuel cells in heavy-duty transportation, Nat. Energy 6 (2021) 462-474.

[2] L. Huang, S. Zaman, X.L. Tian, Z.T. Wang, W.S. Fang, B.Y. Xia, Advanced platinum-based oxygen reduction electrocatalysts for fuel cells, Acc. Chem. Res. 54 (2021) 311-322.

[3] K. Kodama, T. Nagai, A. Kuwaki, R. Jinnouchi, Y. Morimoto, challenges in applying highly active Pt-based nanostructured catalysts for oxygen reduction reactions to fuel cell vehicles, Nat. Nanotech. 16 (2021) 140-147.

[4] Y.L. Ma, A.N. Kuhn, W.P. Gao, T. Al-Zoubi, H. Du, X.Q. Pan, H. Yang, Strong electrostatic adsorption approach to the synthesis of sub-three nanometer intermetallic platinum-cobalt oxygen reduction catalysts, Nano Energy 79 (2021) 105465.

[5] L. Du, V. Prabhakaran, X.H. Xie, S. Park, Y. Wang, Y.Y. Shao, Low-PGM and PGM-free catalysts for proton exchange membrane fuel cells: stability challenges and material solutions, Adv. Mater. 33 (2021) 1908232.

[6] J. Du, J. Quinson, D.M. Zhang, F. Bizzotto, A. Zana, M. Arenz, Bifunctional Pt-IrO_2 catalysts for the oxygen evolution and oxygen reduction reactions: alloy nanoparticles versus nanocomposite catalysts, ACS Catal. 11 (2021) 820-828.

[7] S. Akula, P. Varathan, R.S. Menon, A.K. Sahu, Rationally constructing nitrogen–fluorine heteroatoms on porous carbon derived from pomegranate fruit peel waste towards an efficient oxygen reduction catalyst for polymer electrolyte membrane fuel cells, Sustain. Energy Fuels 5 (2021) 886-899.

[8] S. Akula, A.K. Sahu, Structurally modulated graphitic carbon nanofiber and heteroatom (N,F) engineering toward metal-free ORR electrocatalysts for polymer electrolyte membrane fuel cells, ACS Appl. Mater. Interfaces 12 (2020) 11438-11449.

[9] S. Akula, B. Balasubramaniam, P. Varathan, A.K. Sahu, Nitrogen−fluorine dual doped porous carbon derived from silk cotton as efficient oxygen reduction catalyst for polymer electrolyte fuel cells, ACS Appl. Energy Mater. 2 (2019) 3253-3263.

[10] F. Luo, A.R. Roy, L. Silvioli, D.A. Cullen, A. Zitolo, M.T. Sougrati, I.C. Oguz, T. Mineva, D. Teschner, S. Wagner, J. Wen, F. Dionigi, U.I. Kramm, J. Rossmeisl, F. Jaouen, P. Strasser, P-block single-metal-site tin/nitrogen-doped carbon fuel cell cathode catalyst for oxygen reduction reaction, Nat. Mater. 19 (2020) 1215–1223.

[11] J. Lilloja, E. Kibena-Põldsepp, A. Sarapuu, A. Kikas, V. Kisand, M. Käärik, M. Merisalu, A. Treshchalov, J. Leis, V. Sammelselg, Q. Wei, S. Holdcroft, K. Tammeveski, Nitrogen-

doped carbide-derived carbon/carbon nanotube composites as cathode catalysts for anion exchange membrane fuel cell application. Appl. Catal. B: Environ. 272 (2020) 119012.

[12] Q. Gao, Y. Wang, M. Yang, W. Shen, Y.M. Jiang, R.X. He, M. Li, N, S-codoped porous carbon as metal-free electrocatalyst for oxygen reduction reaction, J. Solid State Electrochem. 25 (2021) 1765-1773.

[13] T. Marshall-Roth, N.J. Libretto, A.T. Wrobel, K.J. Anderton, M.L. Pegis, N.D. Ricke, T. Van Voorhis, J.T. Miller, Y. Surendranath, A pyridinic Fe-N_4 macrocycle models the active sites in Fe/N-doped carbon electrocatalysts, Nat. Commun. 11 (2020) 5283.

[14] A. Sarapuu, E. Kibena-Põldsepp, M. Borghei, K. Tammeveski, Electrocatalysis of oxygen reduction on heteroatom-doped nanocarbons and transition metal–nitrogen–carbon catalysts for alkaline membrane fuel cells, J. Mater. Chem. A 6 (2018) 776-804.

[15] J.K. Li, M.T. Sougrati, A. Zitolo, J.M. Ablett, I.C. Oguz, T. Mineva, I. Matanovic, P. Atanassov, Y. Huang, I. Zenyuk, A. Di Cicco, K. Kumar, L. Dubau, F. Maillard, G. Drazic, F. Jaouen, Identification of durable and non-durable FeNx sites in Fe–N–C materials for proton exchange membrane fuel cells, Nat. Catal. 4 (2021) 10–19.

[16] J. Lilloja, E. Kibena-Põldsepp, A. Sarapuu, M. Kodali, Y.C. Chen, T. Asset, M. Käärik, M. Merisalu, P. Paiste, J. Aruväli, A. Treshchalov, M. Rähn, J. Leis, V. Sammelselg, S. Holdcroft, P. Atanassov, K. Tammeveski, Cathode catalysts based on cobalt and nitrogen-doped nanocarbon composites for anion exchange membrane fuel cells, ACS Appl. Energy Mater. 3 (2020) 5375-5384.

[17] S. Specchia, P. Atanassov, J.H. Zagal, Mapping transition metal–nitrogen–carbon catalyst performance on the critical descriptor diagram, Curr. Opin. Electrochem. 27 (2021) 10068.

[18] H.P. Rong, S.F. Ji, J.T. Zhang, D.S. Wang, Y.D. Li, Synthetic strategies of supported atomic clusters for heterogeneous catalysis, Nat. Commun. 11 (2020) 5884.

[19] Q. Wang, Y.Q. Yang, F.F. Sun, G.B. Chen, J. Wang, L.S. Peng, W.T. Chen, L. Shang, J.Q. Zhao, D. Sun-Waterhouse, T.R. Zhang, G.I.N. Waterhouse, Molten NaCl-assisted synthesis of porous Fe-N-C electrocatalysts with a high density of catalytically accessible FeN_4 active sites and outstanding oxygen reduction reaction performance, Adv. Energy Mater. 11 (2021) 2100219.

[20] S. Ratso, A. Zitolo, M. Kaarik, M. Merisalu, A. Kikas, V. Kisand, M. Rähn, P. Paiste, J. Leis, V. Sammelselg, S. Holdcroft, F. Jaouen, K. Tammeveski, Non-precious metal cathodes for anion exchange membrane fuel cells from ball-milled iron and nitrogen doped carbide-derived carbons, Renewable Energy 167 (2021) 800-810.

[21] Y.C. Li, X.F. Liu, L.R. Zheng, J.X. Shang, X. Wan, R.M. Hu, X. Guo, S. Hong, J.L. Shui, Preparation of Fe–N–C catalysts with FeNx (x = 1, 3,4) active sites and comparison of their activities for the oxygen reduction reaction and performances in proton exchange membrane fuel cells, J. Mater. Chem. A 7 (2019) 26147-26153.

[22] L. Wang, X. Wan, S.Y. Liu, L. Xu, J.L. Shui, Fe-N-C catalysts for PEMFC: Progress towards the commercial application under DOE reference, J. Energy Chem. 39 (2019) 77-87.

[23] R. Sibul, E. Kibena-Põldsepp, S. Ratso, M. Kook, M.T. Sougrati, M. Käärik, M. Merisalu, J. Aruväli, P. Paiste, A. Treshchalov, J. Leis, V. Kisand, V. Sammelselg, S. Holdcroft, F. Jaouen, K. Tammeveski, Iron- and nitrogen-doped graphene-based catalysts for fuel cell application, ChemElectroChem 7 (2020) 1739-1747.

[24] T. Asset, P. Atanassov, Iron-nitrogen-carbon catalysts for proton exchange membrane fuel cells, Joule 4 (2020) 33-44.

[25] C.H. Choi, C. Baldizzone, J.P. Grote, A.K. Schuppert, F. Jaouen, K.J.J. Mayrhofer, Stability of Fe-N-C catalysts in acidic medium studied by Operando Spectroscopy, Angew. Chem. Int. Ed. 54 (2015) 12753 –12757.

[26] D. Shin, S. Bhandari, M.F. Tesch, S. A. Bonke, F. Jaouen, S. Chabbra, C. Pratsch, A. Schnegg, A.K. Mechler, Reduced formation of peroxide and radical species stabilises iron-based hybrid catalysts in polymer electrolyte membrane fuel cells, J. Energy Chem. 65 (2022) 433-438.

[27] Y. Wang, M. J. Larsen, S. Rojas, M.T. Sougrati, F. Jaouen, P. Ferrer, D. Gianolio, S. Berthon-Fabry, Influence of the synthesis parameters on the proton exchange membrane fuel cells performance of Fe–N–C aerogel catalysts J. Power Sources 514 (2021) 230561.

[28] D. Malko, A. Kucernak, T. Lopes, In situ electrochemical quantification of active sites in Fe–N/C non-precious metal catalysts, Nat. Commun. 7 (2016) 13285.

[29] V.A. Saveleva, K. Ebner, L. Ni, G. Smolentsev, D. Klose, A. Zitolo, E. Marelli, J. Li, M. Medarde, O.V. Safonova, M. Nachtegaal, F. Jaouen, U.I. Kramm, T.J. Schmidt, J. Herranz, Potential-induced spin changes in Fe/N/C electrocatalysts assessed by in situ X-ray Emission Spectroscopy, Angew. Chem. Int. Ed. 60 (2021) 11707-11712.

[30] S. Ratso, M. Kaarik, M. Kook, P. Paiste, V. Kisand, S. Vlassov, J. Leis, K. Tammeveski, Iron and nitrogen co-doped carbide-derived carbon and carbon nanotube composite catalysts for oxygen reduction reaction, ChemElectroChem 5 (2018) 1827-1836.

[31] R.G. Wang, Y.Y. Yang, Y. Zhao, L.J. Yang, P.F. Yin, J. Mao, T. Ling, Multiscale structural engineering of atomically dispersed FeN_4 electrocatalyst for proton exchange membrane fuel cells, J. Energy Chem. 58 (2021) 629-635.

[32] S. Wagner, H. Auerbach, C.E. Tait, I. Martinaiou, S.C.N. Kumar, C. Kubel, I. Sergeev, H.C. Wille, J. Behrends, J.A. Wolny, V. Schunemann, U.I. Kramm, Elucidating the structural composition of an Fe–N–C catalyst by nuclear- and electron-resonance techniques, Angew. Chem. Int. Ed. 58 (2019) 10486-10492.

[33] A. Zitolo, V. Goellner, V. Armel, M.T. Sougrati, T. Mineva, L. Stievano, E. Fonda, F. Jaouen, Identification of catalytic sites for oxygen reduction in iron- and nitrogen-doped graphene materials, Nat. Mater. 14 (2015) 937–942.

[34] R. Sgarbi, K. Kumar, F. Jaouen, A. Zitolo, E.A. Ticianelli, F. Maillard, Oxygen reduction reaction mechanism and kinetics on M-N_xC_y and M@N-C active sites present in model M-N-C catalysts under alkaline and acidic conditions, J. Solid State Electrochem. 25 (2021) 45–56.

[35] R. Praats, M. Kaarik, A. Kikas, V. Kisand, J. Aruvali, P. Paiste, M. Merisalu, J. Leis, V. Sammelselg, J.H. Zagal, S. Holdcroft, N. Nakashima, K. Tammeveski, Electrocatalytic oxygen reduction reaction on iron phthalocyanine modified carbide-derived carbon/carbon nanotube composite electrocatalysts, Electrochim. Acta 334 (2020) 135575.

[36] F. Xiao, X. Liu, C.J. Sun, I.H. Hwang, Q. Wang, Z.W. Xu, Y.A. Wang, S.Q. Zhu, H.W. Wu, Z.D. Wei, L.P. Zheng, D.J. Cheng, M. Gu, G.L. Xu, K. Amine, M.H. Shao, Solid-state synthesis of highly dispersed nitrogen-coordinated single iron atom electrocatalysts for proton exchange membrane fuel cells, Nano Lett. 21 (2021) 3633-3639.

[37] Y. Wu, J. Huang, Z. Lin, L. Li, G. Liang, Y.Q. Jin, G. Huang, H. Zhang, J. Chen, F. Xie, Y. Jin, N. Wang, H. Meng, Fe-Nx doped carbon nanotube as a high efficient cathode catalyst for proton exchange membrane fuel cell, Chem. Eng. J. 423 (2021) 130241.

[38] L. Jiao, J. Li, L. LaRochelle Richard, Q. Sun, T. Stracensky, E. Liu, M.T. Sougrati, Z. Zhao, F. Yang, S. Zhong, H. Xu, S. Mukerjee, Y. Huang, D.A. Cullen, J.H. Park, M.

Ferrandon, D.J. Myers, F. Jaouen, Q. Jia, Chemical vapour deposition of Fe–N–C oxygen reduction catalysts with full utilization of dense Fe–N_4 sites, Nat. Mat. 20 (2021) 1385-1391.

[39] M. Paz Oyarzún, N. Silva, D. Cortes-Arriagad, J.F. Silva, I.O. Ponce, M. Flores, K. Tammeveski, D. Bélanger, A. Zitolo, F. Jaouen, J.H. Zagal, Enhancing the electrocatalytic activity of Fe phthalocyanines for the oxygen reduction reaction by the presence of axial ligands: Pyridine-functionalized single-walled carbon nanotubes, Electrochim. Acta, 398 (2021) 139263.

[40] Y. Lin, K. Liu, K. Chen, Y. Xu, H. Li, J. Hu, Y.R. Lu, T.S. Chan, X. Qiu, J. Fu, M. Liu, Tuning charge distribution of FeN_4 via external N for enhanced oxygen reduction reaction, ACS Catal. 11 (2021) 6304−6315.

[41] H. Oschinski, A. Morales-Garcia, F. Illas, Interaction of first row transition metals with M_2C (M = Ti, Zr, Hf, V, Nb, Ta, Cr, Mo, and W) MXenes: a quest for single-atom catalysts, J. Phys. Chem. C 125 (2021) 2477-2484.

[42] H.S. Kim, C.H. Lee, J.H. Jang, M.S. Kang, H. Jin, K.S. Lee, S.U. Lee, S.J. Yoo, W.C. Yoo, Single-atom oxygen reduction reaction electrocatalysts of Fe, Si, and N co-doped carbon with 3D interconnected mesoporosity, J. Mater. Chem. A 9 (2021) 4297-4309.

[43] M.T. Darby, M. Stamatakis, Single-atom alloys for the electrochemical oxygen reduction reaction, ChemPhysChem 22 (2021) 499-508.

[44] F. Luo, S. Wagner, I. Onishi, S. Selve, S. Li, W. Ju, H. Wang, J. Steinberg, A. Thomas, U.I. Kramm, P. Strasser, Surface site density and utilization of platinum group metal (PGM)-free Fe–NC and FeNi–NC electrocatalysts for the oxygen reduction reaction, Chem. Sci. 12 (2021) 384-396.

[45] G.G. Yang, J.W. Zhu, P.F. Yuan, Y.F. Hu, G. Qu, B.A. Lu, X.Y. Xue, H.B. Yin, W.Z. Cheng, J.Q. Cheng, W.J. Xu, J. Li, J.S. Hu, S.C. Mu, J.N. Zhang, Regulating Fe-spin state by atomically dispersed Mn-N in Fe-N-C catalysts with high oxygen reduction activity, Nat. Commun. 12 (2021) 1734.

[46] Y. Cheng, J.Y. Zhang, X. Wu, C.J. Tang, S.Z. Yang, P.P. Su, L. Thomsen, F.P. Zhao, S.F. Lu, J. Liu, S.P. Jiang, A template-free method to synthesis high density iron single atoms anchored on carbon nanotubes for high temperature polymer electrolyte membrane fuel cells, Nano Energy 80 (2021) 105534.

[47] M. Mazzucato, G. Daniel, A. Mehmood, T. Kosmala, G. Granozzi, A. Kucernak, C. Durante, Effects of the induced micro- and meso-porosity on the single site density and turn over frequency of Fe-N-C carbon electrodes for the oxygen reduction reaction, Appl. Catal. B: Environ. 291 (2021) 120068.

[48] A. Mehmood, B. Ali, M. Gong, M.G. Kim, J.Y. Kim, J.H. Bae, A. Kucernak, Y.M. Kang, K.W. Nam, Development of a highly active Fe-N-C catalyst with the preferential formation of atomic iron sites for oxygen reduction in alkaline and acidic electrolytes, J. Colloid Interface Sci. 596 (2021) 148-157.

[49] G. Daniel, T. Kosmala, F. Brombin, M. Mazzucato, A. Facchin, M.C. Dalconi, D. Badocco, P. Pastore, G. Granozzi, C. Durante, Highly graphitized Fe-N-C electrocatalysts prepared from chitosan hydrogel Frameworks, Catalysts 11 (2021) 390.

[50] E. Proietti, F. Jaouen, M. Lefevre, N. Larouche, J. Tian, J. Herranz, J.P. Dodelet, Iron-based cathode catalyst with enhanced power density in polymer electrolyte membrane fuel cells, Nat. Commun. 2 (2011) 416.

[51] T.J. Zhang, A.G. Walsh, J.H. Yu, P. Zhang, Single-atom alloy catalysts: structural analysis, electronic properties and catalytic activities, Chem. Soc. Rev. 50 (2021) 569-588.

[52] A. Garcia, L. Pascual, P. Ferrer, D. Gianolio, G. Held, D.C. Grinter, M.G.A. Pena, M. Retuerto, S. Rojas, Study of the evolution of FeN_xC_y and Fe_3C species in Fe/N/C catalysts during the oxygen reduction reaction in acid and alkaline electrolyte, J. Power Sources 490 (2021) 229487.

[53] W.H. Zhong, Y. Qiu, H.J. Shen, X.J. Wang, J.Y. Yuan, C.Y. Jia, S.W. Bi, J. Jiang, Electronic Spin Moment As a catalytic descriptor for Fe single-atom catalysts supported on C_2N, J. Am. Chem. Soc. 143 (2021) 4405-4413.

[54] R.X. Wang, Y.L. Yuan, J.B. Zhang, X.C. Zhong, J.M. Liu, Y.M. Xie, S.P. Zhong, Z.F. Xu, Embedding Fe_2P nanocrystals in bayberry-like N, P-enriched carbon nanospheres as excellent oxygen reduction electrocatalyst for zinc-air battery, J. Power Sources 501 (2021) 230006.

[55] B. Singh, V. Sharma, R.P. Gaikwad, P. Fornasiero, R. Zboril, M.B. Gawande, Single-atom catalysts: a sustainable pathway for the advanced catalytic applications, Small 17 (2021) 2006473.

[56] C. Gallenkamp, U.I. Kramm, V. Krewald, Spectroscopic discernibility of dopants and axial ligands in pyridinic FeN_4 environments relevant to single-atom catalysts, Chem. Commun. 57 (2021) 859-862.

[57] M. Jafari, H. Gharibi, M.J. Parnian, M. Nasrollahpour, M. Vafaee, Iron-nanoparticle-loaded nitrogen-doped carbon nanotube/carbon sheet composites derived from MOF as electrocatalysts for an oxygen reduction reaction, ACS Appl. Nano Mater. 4 (2021) 459-477.

[58] T. Reshetenko, G. Randolf, M. Oddgaard, B. Zulevi, A. Serov, A. Kulikovsky, The effect of proton conductivity of Fe–N–C–based cathode on PEM fuel cell performance, J. Electrochem. Soc. 167 (2020) 084501.

[59] V.C.A. Ficca, C. Santoro, A. D'Epifanio, S. Licoccia, A. Serov, P. Atanassov, B. Mecheri, Effect of active site poisoning on iron-nitrogen-carbon platinum-group-metal-free oxygen reduction reaction catalysts operating in neutral media: a rotating disk electrode study, ChemElectroChem 7 (2020) 3044-3055.

[60] T. Reshetenko, A. Serov, M. Odgaard, G. Randolf, L. Osmieri, A. Kulikovsky, Electron and proton conductivity of Fe-N-C cathodes for PEM fuel cells: A model-based electrochemical impedance spectroscopy measurement, Electrochem. Commun. 118 (2020) 106795.

[61] J. Lilloja, M. Mooste, E. Kibena-Põldsepp, A. Sarapuu, B. Zulevi, A. Kikas, H.M. Piirsoo, A. Tamm, V. Kisand, S. Holdcroft, A. Serov, K. Tammeveski, Mesoporous iron-nitrogen co-doped carbon material as cathode catalyst for the anion exchange membrane fuel cell, J Power Sources Adv. 8 (2021) 100052.

[62] D.R. Baker, D.A. Caulk, K.C. Neyerlin, M.W. Murphy, Measurement of oxygen transport resistance in PEM fuel cells limiting current methods, J. Electrochem. Soc. 156 (2009) B991.

[63] T.V. Reshetenko, G. Bender, K. Bethune, R. Rocheleau, Systematic study of back pressure and anode stoichiometry effects on spatial PEMFC performance distribution, Electrochim. Acta 56 (2011) 8700-8710.

[64] T.R. Ralph, M.P. Hogarth, Catalysis for low temperature fuel cells, Platinum Met. Rev., 46 (2002) 117-135.

[65] A.C. Ferrari, J. Robertson, Interpretation of Raman spectra of disordered and amorphous carbon, Phys. Rev. B 61 (2000) 14095-14107.

[66] F.J. Sotomayor, K.A. Cychosz, M. Thommes, Characterization of micro/mesoporous materials by physisorption: concepts and case studies, Acc. Mater. Surf. Res. 3 (2018) 34-50.

[67] C.S. Saurav, V. Mishra, V. Vemuri, S.C. Peter, "Breaking the O=O Bond": Deciphering the role of each element in highly durable $CoPd_2Se_2$ toward oxygen reduction reaction ACS Appl. Energy Mater. 3 (2020) 231-239.

[68] H. Jiang, J. Gu, X. Zheng, M. Liu, X. Qiu, L. Wang, W. Li, Z. Chen, X. Ji, J. Li, Defect-rich and ultrathin N doped carbon nanosheets as advanced trifunctional metal-free electrocatalysts for the ORR, OER and HER, Energy Environ. Sci. 12 (2019) 322-333.

[69] Y.C. Wang, F.L. Chu, J. Zeng, Q.J. Wang, T.Y. Naren, Y.Y. Li, Y. Cheng, Y.P. Lei, F.X. Wu, Single atom catalysts for fuel cells and rechargeable batteries: principles, advances, and opportunities, ACS Nano 15 (2021) 210-239.

[70] T. Reshetenko, A. Serov, A. Kulikovsky, P. Atanassov, Impedance spectroscopy characterization of PEM cells with Fe-N-C-based cathodes, J. Electrochem. Soc. 166 (2019) F653.

[71] USA DOE Annual Merit Review 2021: P. Zelenay and D. Myers https://www.hydrogen.energy.gov/pdfs/review21/fc160_myers_zelenay_2021_o.pdf

Figures

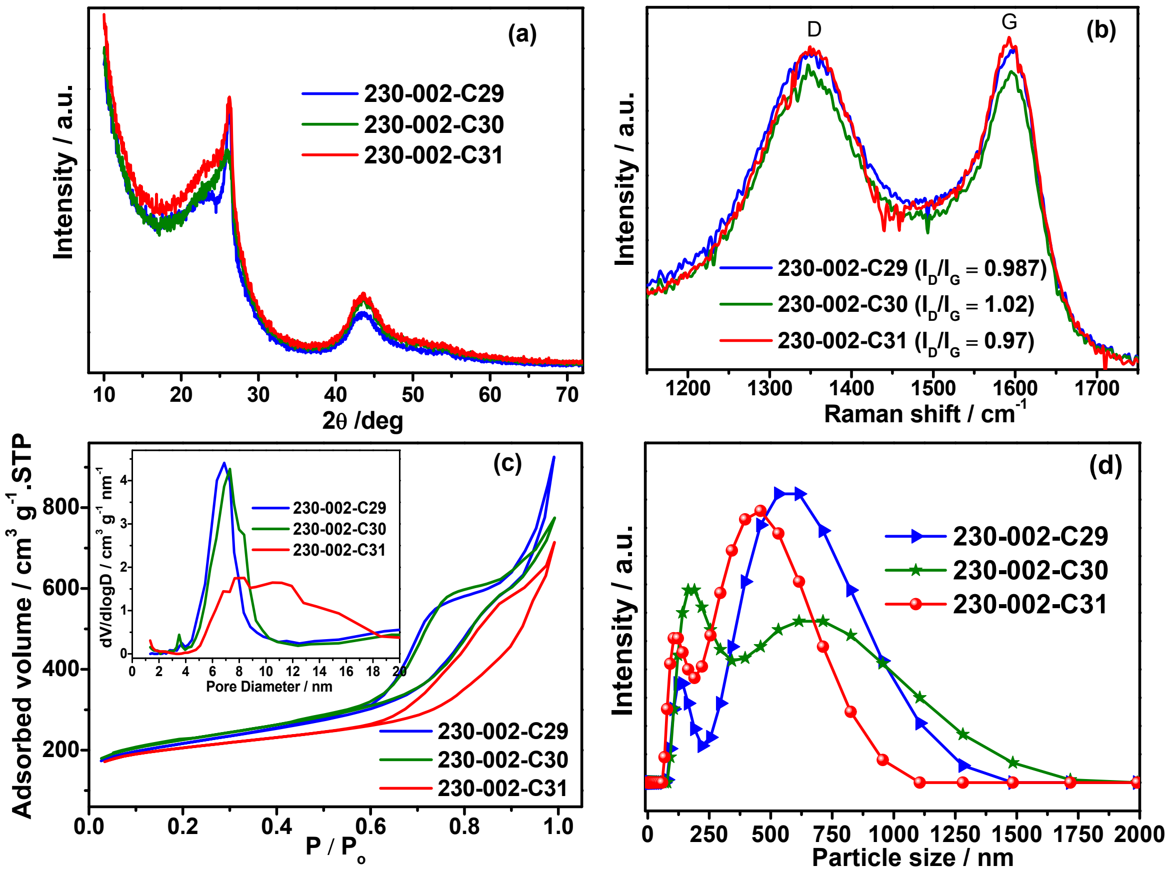

Fig. 1. (a) XRD patterns, (b) Raman spectra, (c) N_2 physisorption isotherms and pore size distribution (inset) and (d) particle size distribution of the Fe-N-C catalysts.

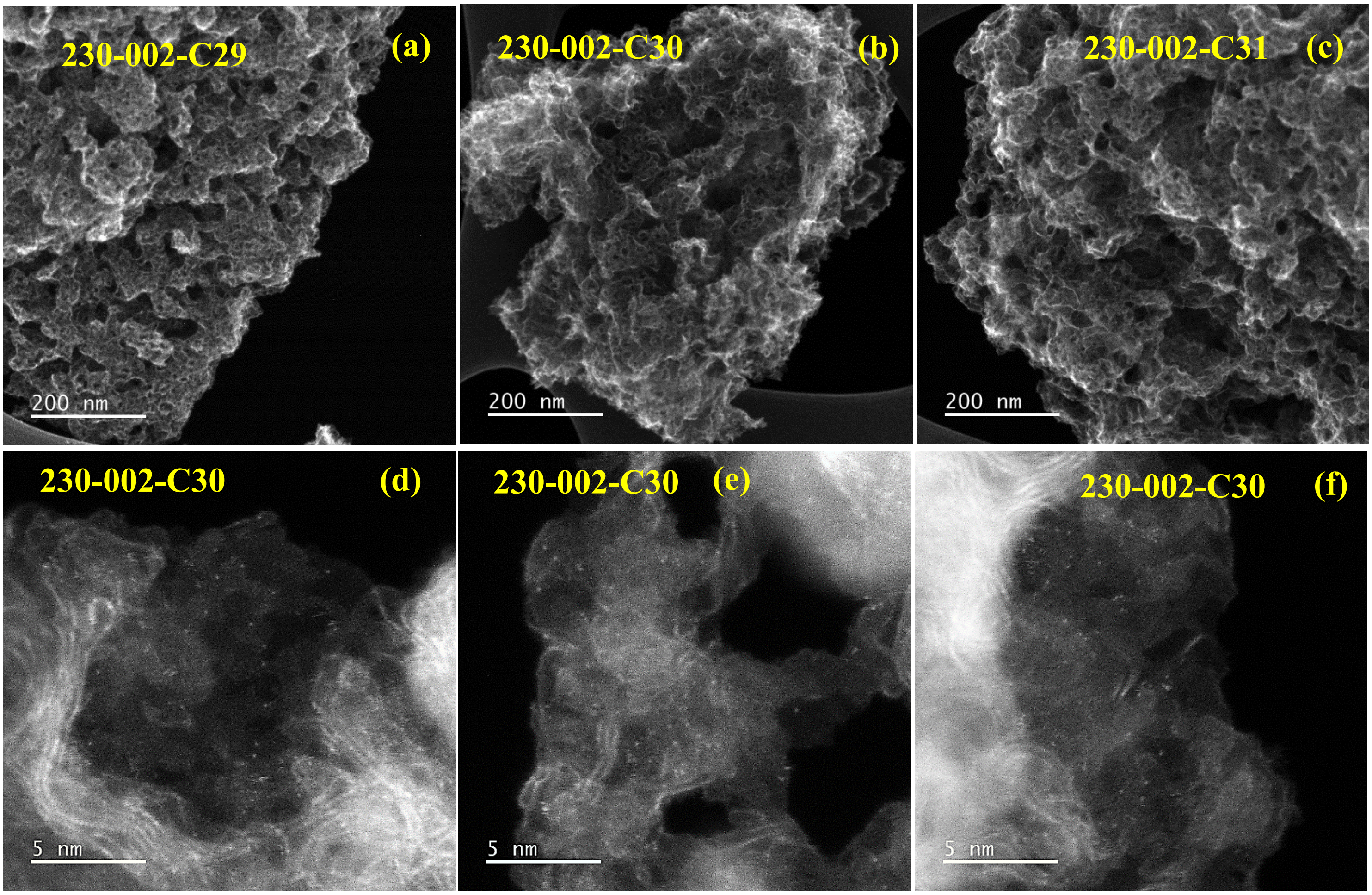

Fig. 2. SE-STEM images of (a) 230-002-C29, (b) 230-002-C30, (c) 230-002-C31 catalysts respectively; (d, e, f) ADF-STEM images showing high abundance of atomically dispersed Fe sites for 230-002-C30.

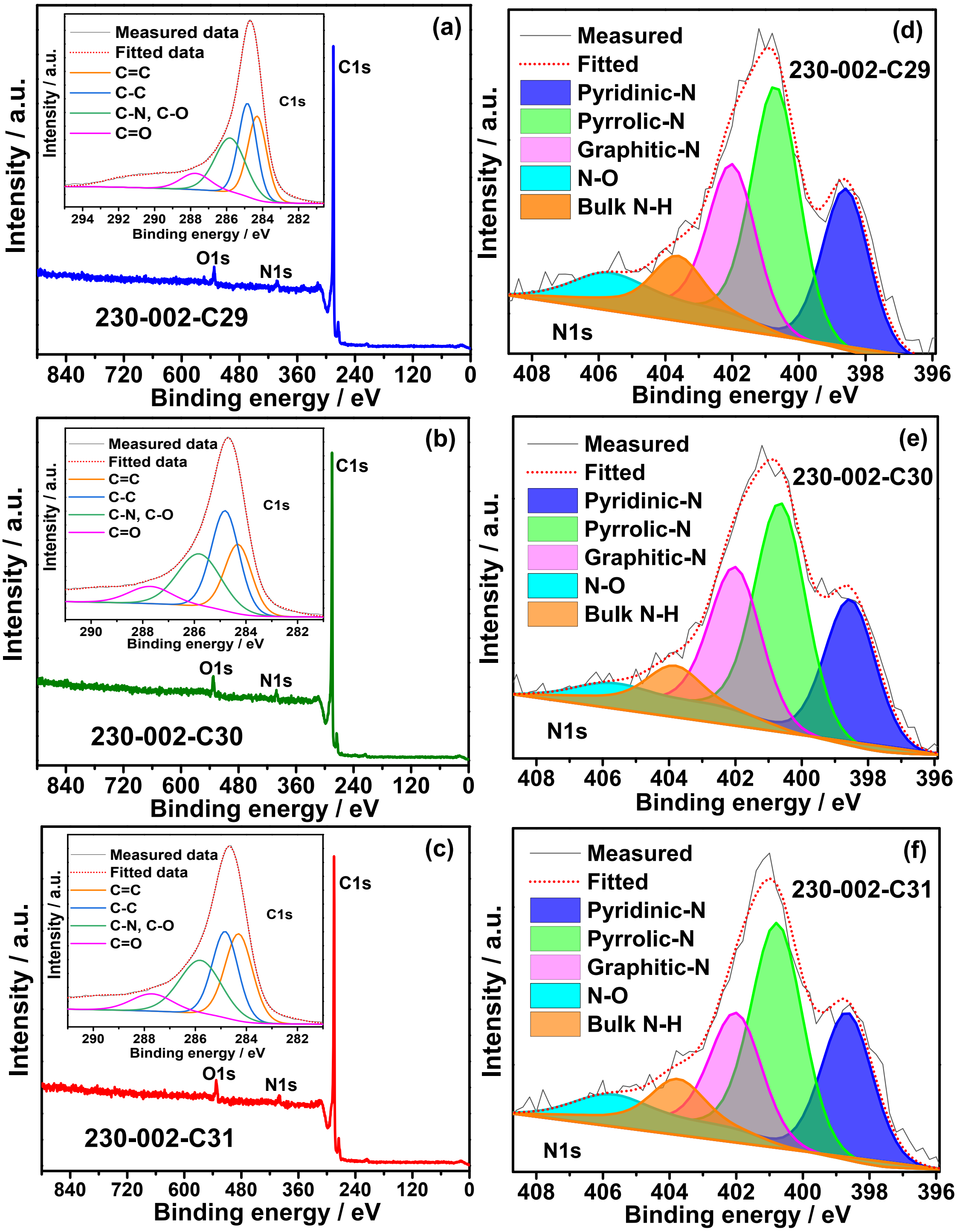

Fig. 3. XPS analysis of the catalysts: (a, b, c) wide scan spectra of 230-002-C29, 230-002-C30, and 230-002-C31 samples, respectively. Core-level spectra in the C1s region for various functional groups are fitted in the insets. (d, e, f) N1s deconvoluted spectra of Fe-N-C catalysts.

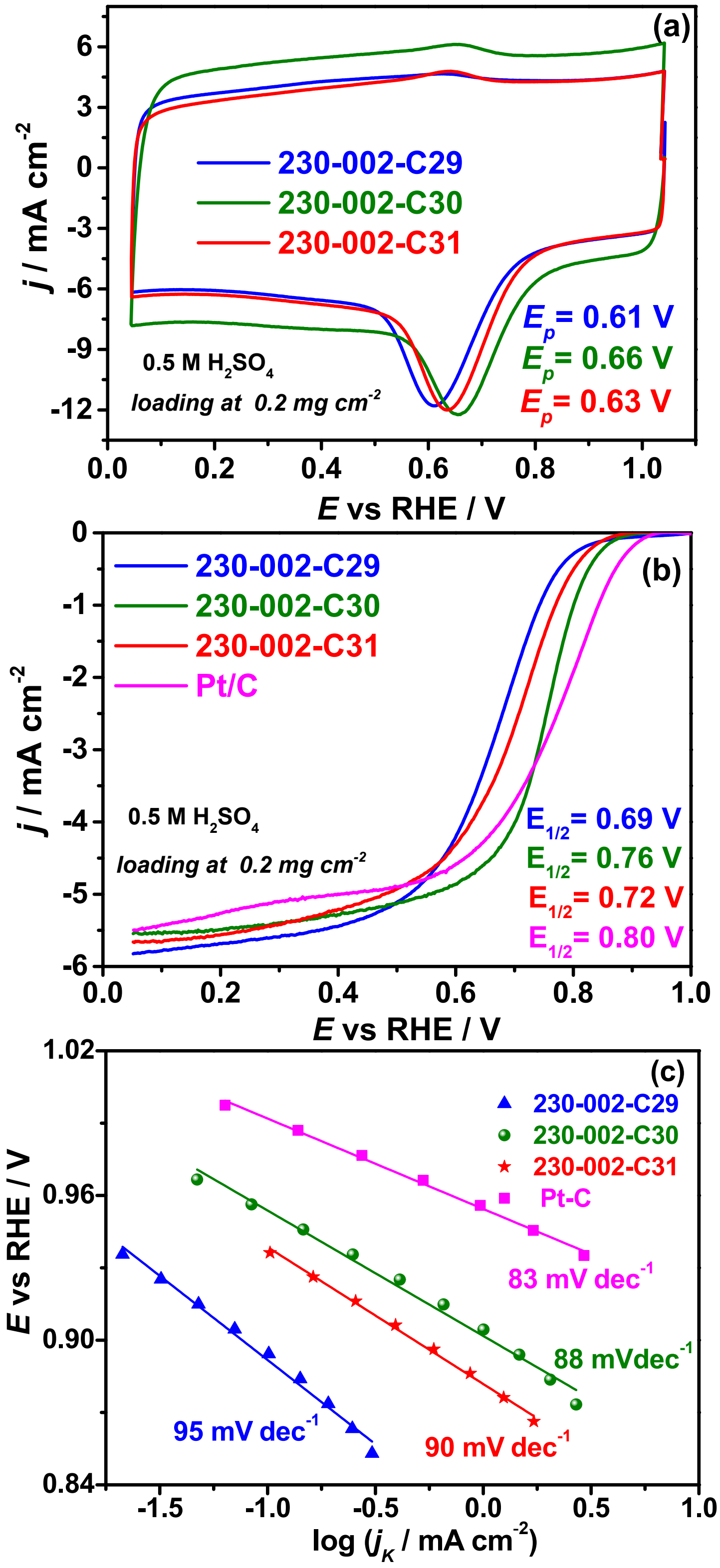

Fig. 4. (a) CVs of Fe-N-C and (b) LSVs of Fe-N-C and Pt/C catalysts measured in O_2-saturated 0.5 M H_2SO_4 electrolyte solution at 100 and 10 mV s^{-1} scan rates, respectively; LSVs recorded at 1900 rpm, (c) Tafel plots for ORR of the catalysts with corresponding slope values.

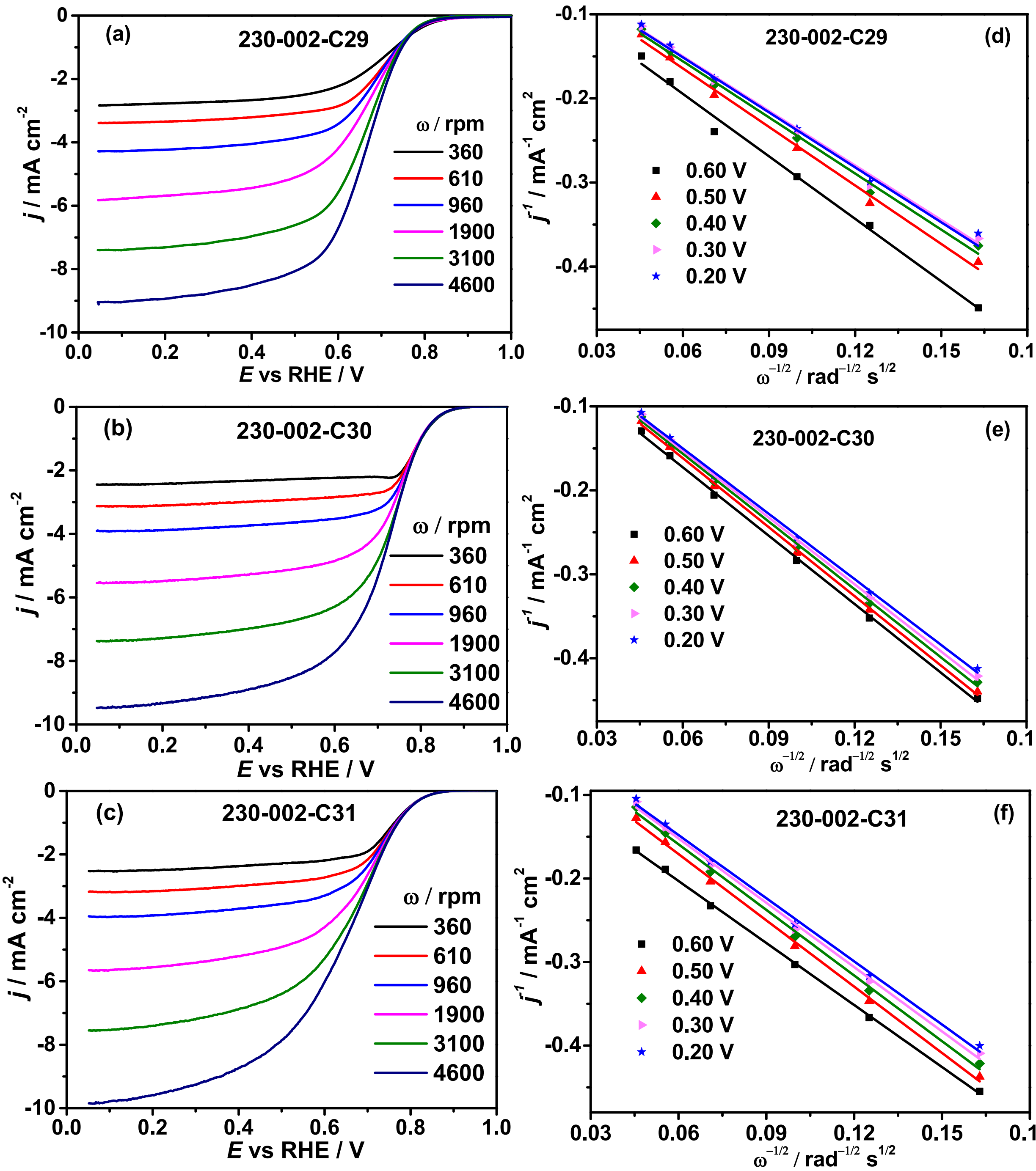

Fig. 5. (a, b, c) hydrodynamic voltammograms of the Fe-N-C catalysts measured in O_2-saturated 0.5 M H_2SO_4 electrolyte solution at 10 mV s^{-1}; (d, e, f) the respective K-L plots for oxygen reduction on the Fe-N-C catalysts at various potentials.

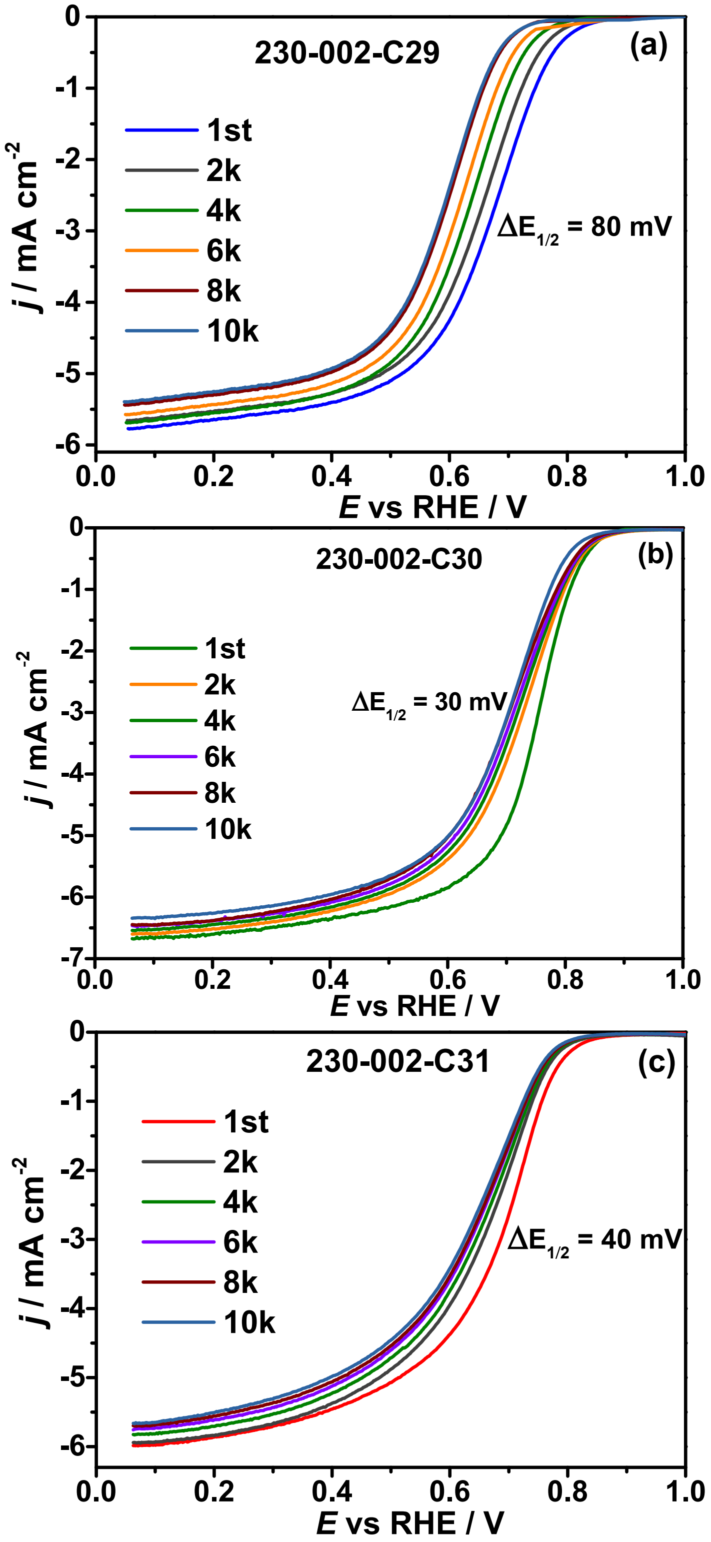

Fig. 6. LSVs of the catalysts after the 10,000-potential cycling. (a) 230-002-C29, (b) 230-002-C30 and (c) 230-002-C31. LSVs measured at each 2000 cycles at 1900 rpm in O_2-saturated 0.5 M H_2SO_4 solution at 10 mV s^{-1}; the corresponding change in the $E_{1/2}$ values are indicated.

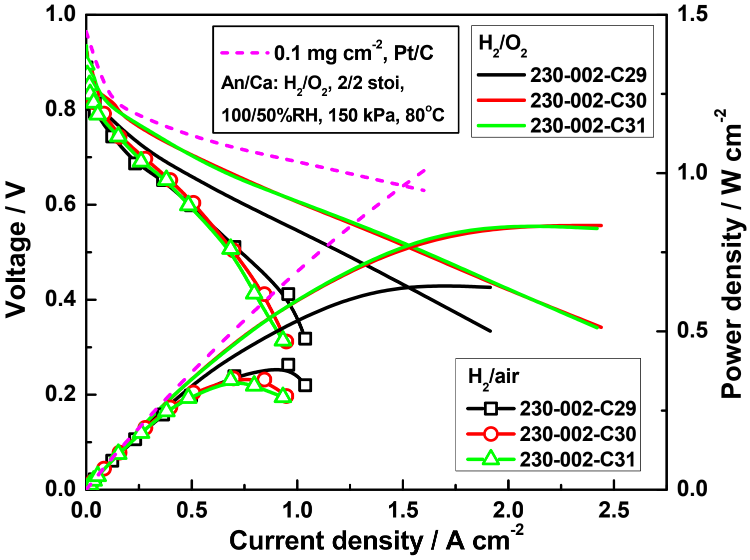

Fig. 7. Polarization and power density curves for MEAs with Fe-N-C and Pt/C cathodes using O_2 and air as cathode feed gases.

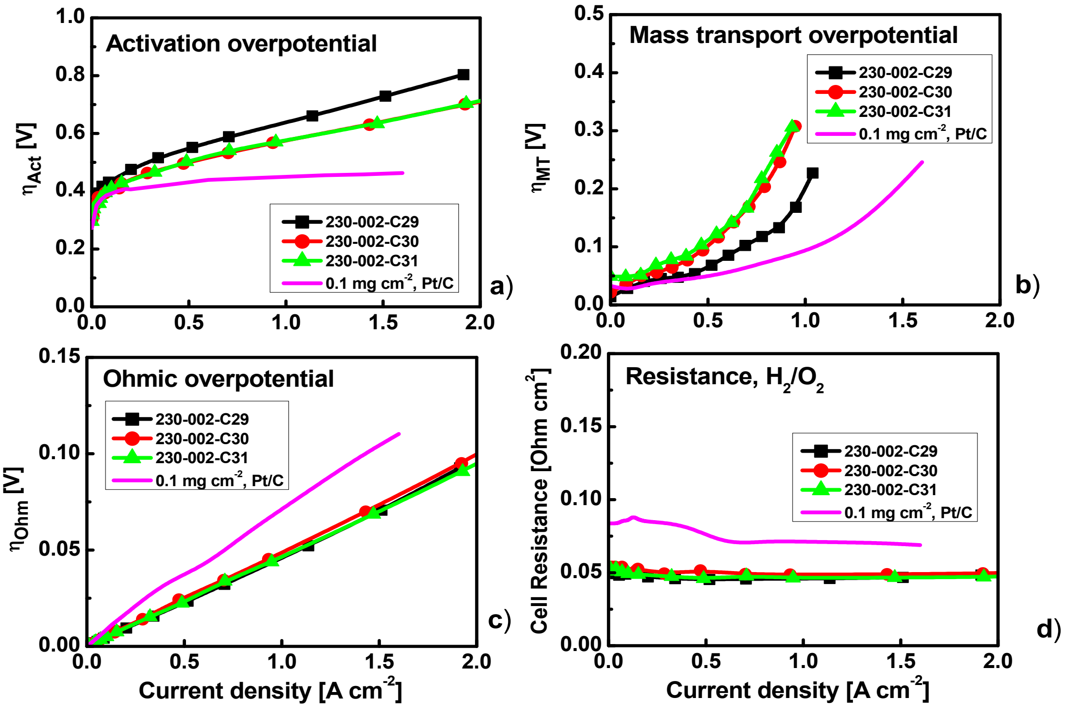

Fig. 8. Activation (a), mass transport (b) and ohmic (c) voltage losses; cell resistance values (d) for PGM-free and Pt MEAs.

Table 1. Physical parameters of the catalysts; values obtained from XRD, Raman spectroscopy, DLS and N_2 physisorption analysis.

	230-002-C29	**230-002-C30**	**230-002-C31**
XRD @ 23.5 θ (°) (crystallite size) (nm)	0.734	1.2	3
DLS (nm)	520	355	270
Raman: I_D/I_G ratio	0.96	1.02	0.98
BET (m²/g)	700	725	640
Average pore size (nm)	7	7	8
pH	10.01	9.75	9.75

Graphical abstract